49th AIAA Aerospace Sciences Meeting including the New Horizons Forum and Aerospace Exposition
4 - 7 January 2011, Orlando, Florida

AIAA 2011-756

Wall-Layer Modeling for Cartesian Grid Solver Using an Overset Boundary Layer Orthogonal Curvilinear Grid

S. Bhushan, A. Hanaoka, J. Yang and F. Stern
IIHR-Hydroscience and Engineering, University of Iowa, Iowa City, IA 52242, USA

Wall-layer modeling for a Cartesian grid solver is developed by coupling an orthogonal curvilinear grid solver using overset grid interpolation and coupled pressure Poisson solver. A thin wall-layer grid is considered sufficient to resolve the boundary layer. Initial validation is performed for laminar flows over a circular cylinder, where the wall-layer model shows up to 10% improvement in the surface pressure and vorticity prediction for *Re* = 40, and 3% improvement in the lift and drag coefficient amplitude for *Re* = 200 compared to the IBM Cartesian grid solver on the same background grid. Next, validation is performed for the turbulent flow over a circular cylinder at *Re* = 3900 using LES. The results show very good agreement for the mean circulation bubble, drag coefficients, unsteady vortex shedding Strouhal number, and mean and turbulent velocity profiles when compared with experimental data and benchmark LES simulations. Initial results for LES of interface piercing circular cylinder at *Re* = 2.7×10^4 and *Fr* = 0.8 are presented. The results are encouraging, but suggests that the current grid is coarse in the normal direction and finer grids are required.

Nomenclature

C_d	=	drag coefficient, i.e., along longitudinal direction
$C_{d,p}$	=	pressure component of the drag coefficient
$C_{d,f}$	=	frictional component of the drag coefficient
C_l	=	lift coefficient, i.e., along transverse direction
D_o	=	diameter of cylinder
E%D	=	error in CFD (*S*) with respect to experimental data (*D*), i.e., (*D*-*S*)/*D*×100
Fr	=	Froude number
P_s	=	surface pressure
Re	=	Reynolds number based on D_o
St	=	Strouhal number fU/D_o, where *f* is vortex shedding frequency and U is inlet velocity
ω_s	=	surface vorticity
X,Y,Z	=	streamwise, transverse and normal directions

I. Introduction

High fidelity solvers are required for the accurate prediction of turbulent flows and should include high order numerical schemes, accurate turbulence closure and better high performance computing (HPC) scalability. The ease of grid generation is also important for complex geometries such as those observed in ship hydrodynamics. Body fitted curvilinear grid solvers have limitations in grid generation. Unstructured grids are comparatively easy to generate, but implementation of higher-order schemes are difficult. Immersed boundary method (IBM) based Cartesian grid solvers involve extremely easy grid generation, allows implementation of higher order schemes and HPC scalability is significantly better than that of the curvilinear and unstructured grid solvers. This makes Cartesian grid solvers well suited for more accurate turbulence simulations such as large eddy simulation (LES) [1]. However, near-wall resolution for such high fidelity solvers is prohibitively expensive for complex geometries. Adaptive/local grid refinement close to the wall may help in reducing the number of grid points, but still are extremely expensive [2]. Further, very small isotropic near-wall grids require very small time steps for unsteady or developing flow. Thus wall-layer (WL) modeling is an important issue for high fidelity Cartesian grid solvers. The objective of this study is to implement a wall-layer model for a high fidelity, IBM based Cartesian grid solver, CFDShip-Iowa V6 (V6-IBM henceforth), developed for ship hydrodynamics applications.

Wall-layer modeling for an IBM based Cartesian grid solver can be performed using wall-functions (WF). Simulations for a ship model DTMB 5415 at straight ahead condition using V6-WF with y^+=30 showed that WF have limitations in accurately predicting flow separation and turbulence quantities [3]. This is expected as WFs are more suited for body fitted grids for which uniform first grid point spacing can be maintained throughout the hull surface. An alternative approach, motivated from the hybrid unsteady Reynolds Averaged Navier Stokes (URANS)/LES modeling approach [4], is to use a body fitted curvilinear grid to resolve boundary layer and Cartesian grid elsewhere. For the boundary layer grid either a linearized Navier-Stokes equation or URANS equations can be solved. The boundary layer solver and background Cartesian grid solvers can be coupled either via boundary conditions, stitched using hybrid grid methods or grid interpolation. Coupling of multi-scale solvers via boundary conditions was performed by Schluter et al. [5] for flows in gas turbine aircraft engine. URANS solver was used for the turbo-machinery portion of the flow and LES solver in combustor. Such approach is suited for grids with aligned boundaries, and is not appropriate for coupling boundary layer and background grids. Zhang et al. [6] proposed a hybrid grid method, where the body fitted curvilinear and adaptive Cartesian background grids were connected using deforming unstructured grid to allow relative motion between the grids. The methodology was applied for 2D compressible and incompressible flows involving multiple bodies in relative motion, such as a fighter aircraft with separating store. However, the hybrid grids can be used only for finite volume approach. Chimera or overset grid methodology [7] allows construction of complex multi-body configurations from sets of relatively simple overlapping grids using appropriate inter-grid communication. This approach is applicable for finite difference solvers and has been previously used for ship hydrodynamics applications by the authors [8].

The overset grid approach provides a framework for interpolating variables between the background and WL grids, and can be applied for velocity and turbulent variables in a straightforward fashion. However, to satisfy mass conservation across the overset grid, pressure Poisson equation is solved in a strongly coupled manner using the PETSc toolkit [9]. For the WL model a body fitted orthogonal curvilinear grid solver (V6-OC) developed by Suh et al. [10] is used, which has the same architecture as V6-IBM. A thin WL grid extending up to y^+~1000 for turbulent flows is considered to maintain orthogonality of the grid.

Initial validation focuses on 2D simulation of laminar flows over a circular cylinder at *Re* = 40 and 200, and results are compared with those obtained using V6-IBM on the same coarse grid, and with benchmark V6-OC, benchmark computational fluid dynamics (CFD) results available in the literature and experimental fluid dynamics (EFD) data. Next, validation study is performed for a turbulent flow at sub-critical *Re* = 3900 using LES based on standard Smagorinsky subgrid-scale model. The results are compared with benchmark V6-OC results and EFD data available in the literature. Validation for surface piercing cylinder at Re=2.7×10^4 and Fr=0.8 is in progress and some preliminary results are presented. The fully converged solutions is expect to be available for the conference presentation. Future work included application of the approach for fixed sinkage and trim Wigley hull simulation at Re=2.2×10^6 and Fr=0.267, which will help evaluate the limitations introduced by orthogonal grid assumption.

II. Numerical Method

A. Governing Equations

The governing equations are incompressible Navier-Stokes equations in absolute inertial earth-fixed coordinates:

$$\frac{\partial \boldsymbol{u}}{\partial t} + \boldsymbol{u} \cdot \nabla \boldsymbol{u} = \frac{1}{\rho} \nabla \cdot (-p\boldsymbol{I} + \boldsymbol{T}) + \boldsymbol{g}, \tag{1}$$

$$\nabla \cdot \boldsymbol{u} = 0, \tag{2}$$

where t is the time, $\boldsymbol{u}$ is the velocity vector, ρ is the density, p is the pressure, $\boldsymbol{I}$ is the unit tensor, $\boldsymbol{g}$ represents the gravity, and $\boldsymbol{T}$ is the stress tensor defined as:

$$\boldsymbol{T} = 2(\nu + \nu_T)\boldsymbol{S}, \tag{3}$$

with ν is the kinematic viscosity, ν_T is the turbulent eddy viscosity and $\boldsymbol{S}$ the strain rate tensor given by

$$\boldsymbol{S} = \frac{1}{2}[\nabla \boldsymbol{u} + (\nabla \boldsymbol{u})^T], \tag{4}$$

where T represents transpose operation. The turbulent eddy viscosity is obtained from either unsteady Reynolds Averaged Navier-Stokes (URANS) or LES turbulence modeling.

The air/water interface is defined as a zero level set of a signed distance function, ϕ, or the level-set function. The interface is tracked by solving level-set evolution equation:

$$\frac{\partial \phi}{\partial t} + \boldsymbol{u} \cdot \nabla \phi = 0, \tag{5}$$

The reinitialization equation for the level-set function is interactively solved to keep ϕ as a signed distance function [13]:

$$\frac{\partial \phi}{\partial \tau} + S(\phi_0)(|\nabla \phi| - 1) = 0, \tag{6}$$

where τ is the pseudo-time for the iteration and $S(\phi_0)$ is the numerically smeared-out function

$$S(\phi_0) = \frac{\phi_0}{\sqrt{{\phi_0}^2 + (\Delta h)^2}}, \tag{7}$$

with ϕ_0 the initial values of ϕ and Δh a small amount, usually the grid cell size, to smear out the sign function.

An interface jump condition in the Navier-Stokes equation is induced by the density and viscosity jump across the interface. A sharp jump is considered for the density, whereas the viscosity is smoothed over a thin transition band across the interface (few grid cells).

B. Cartesian Grid Solver

The governing equations are discretized using finite difference scheme on a non-uniform staggered Cartesian grid and solved using a four-step fractional-step method [1,14] as below:

(1) Predictor:

$$\frac{\hat{u}_i - u_i^n}{\Delta t} = \frac{1}{2}[3A_i^n - A_i^{n-1}] + \frac{1}{2}[C_i^{n+1} + C_i^n] - Grad_i(p^n), \tag{8}$$

(2) First corrector:

$$\frac{u_i^* - \hat{u}_i}{\Delta t} = Grad_i(p^n), \tag{9}$$

(3) Poisson equation:

$$\frac{\partial}{\partial x_i} Grad_i(p^{n+1}) = \frac{1}{\Delta t}\frac{\partial u_i^*}{\partial x_i}, \tag{10}$$

(4) Second corrector:

$$\frac{u_i^{n+1} - u_i^*}{\Delta t} = -Grad_i(p^{n+1}), \tag{11}$$

where superscript n denotes time step, subscript i = 1, 2, 3 represents i-coordinate, $\hat{u}$ and u^* are the first and second intermediate velocities, respectively. $Grad_i(p)$ is a pressure gradient term defined at the center of a cell face (collocated with the i th velocity component). $\boldsymbol{C}$ and $\boldsymbol{A}$ denote the diagonal viscous terms treated by Crank-Nicolson scheme and convection and the other viscous terms treated by Adam-Bashforth scheme, respectively. The diffusion terms and the convection terms are discretized using 2nd central difference scheme and 3rd order QUICK/5th order WENO schemes, respectively. Readers are referred to Yang and Stern [1] for more details.

The turbulence modeling is performed using either blended k-ω/k-ε (BKW) or k-g/k-ε (BKG) models with or without WF for URANS or dynamic Smagorinsky model for LES for low Re simulations. The turbulence equations are solved after the second corrector. The interface modeling is performed using level-set, particle level-set [11] or coupled level-set and volume-of-fluid (CLSVOF) method [12]. This study uses the level-set solver, which uses 3rd

order TVD Runge-Kutta and 5th order WENO schemes. The level-set equations are solved before the momentum equations.

The pressure Poisson equation is solved using the Krylov subspace based multi-grid PETSc library or the semi-coarsening multi-grid HYPRE library. The code uses MPI based domain decomposition for solution on parallel processors and MPI-I/O.

C. Orthogonal Curvilinear Grid Solver

The Cartesian grid solver was recently extended to orthogonal curvilinear grid V6-OC [10], which allows near-wall boundary condition specification. The governing equations are solved in orthogonal curvilinear coordinates, where the velocities are in contra-variant components. The governing equations are solved using finite-difference scheme on staggered grid using the four-step fractional-step methods, as used for V6-IBM. The solver currently provides only dynamic Smagorinsky model turbulence mode for LES. The interface modeling using level-set method/CLSVOF has been implemented and validated. The solver uses the same numerical methods and HPC as used in the V6-IBM solver, including 3rd/5th order convection schemes, multi-grid pressure Poisson solvers and MPI-I/O.

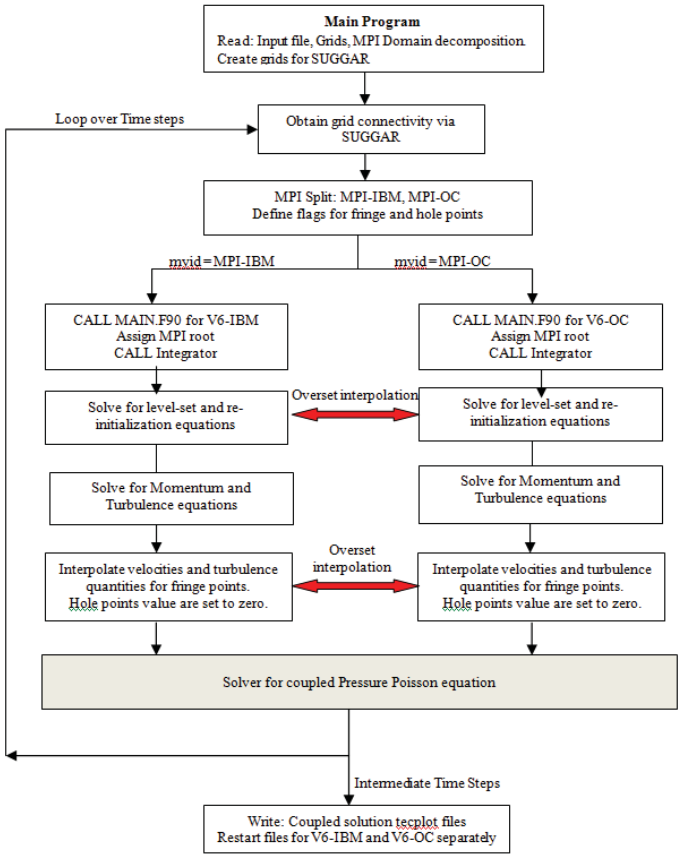

Figure 1. Flow chart demonstrating the steps involved in the coupling V6-IBM and V6-OC solvers.

D. Coupled Curvilinear and Cartesian Grid Solvers

In the coupled curvilinear/Cartesian grid solver (V6.2), both V6-IBM and -OC solvers run simultaneously on separate MPI communicators. Velocities, turbulence quantities, level-set function are interpolated, and the coupled pressure Poisson equation is solved to specify the mass conservation. The flow chart in Fig. 1 demonstrates the solver structure.

The overset grid information is obtained using SUGGAR [7] using the cell centered grids for both the solvers as shown in Fig. 2. SUGGAR currently supports a structure grid function which allows two outermost (JMAX and JMAX-1, herein) planes of the wall-layer grid to be fringe points. The overset grid information file is generated beforehand for the static grids and read as an input file. The file provides the information regarding the fringe points and their donors, and the hole points in the Cartesian grids which are excluded from the solution. For dynamic grids, SUGGAR libraries can be called each time step to update the overset grid information.

The interpolation of velocities, turbulence quantities and level-set function in V6-IBM is similar to the IBM boundary condition specification, and is specified as dirichlet boundary condition for V6-OC. For the velocity interpolation, the contra-variant velocities in V6-OC is first transformed to the Cartesian components, then interpolated at cell centers. The updated velocities at the fringe point for V6-OC are transformed back to the contra-variant components. The values at the staggered grid are obtained using tri-linear interpolation using the surrounding fluid and fringe points for both the solvers. The cell center interpolation of the scalar turbulence quantities and level-set function do not require transformation or staggered grid interpolation. The velocities are interpolated after the predictor, first and second corrector steps, and turbulence and level-set variables are interpolated after the solution of respective equations.

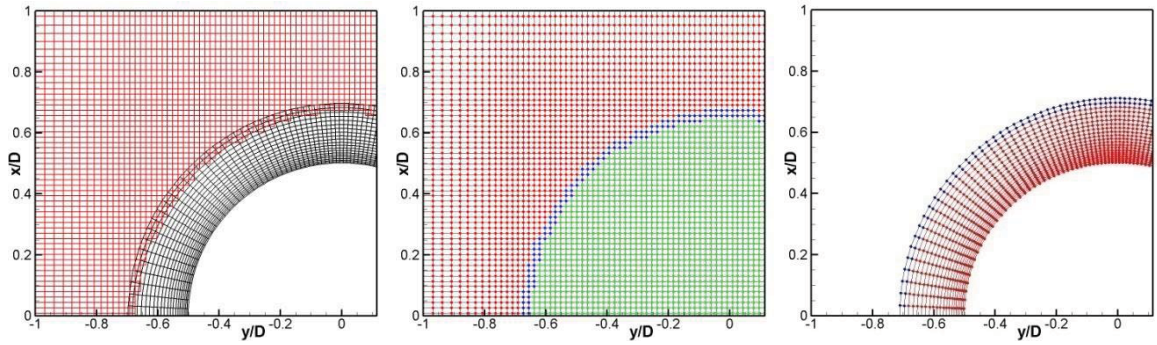

Figure 2. (a) Overset grid configuration for a circular cylinder, (b) fluid points (RED), fringe points (BLUE) and hole points (GREEN) are shown for the Cartesian grid, and (c) fringe and fluid points are shown for the wall-layer grid.

The coupled pressure Poisson equation is solved using PETSc for which the MPI communicator encompasses processors from both the solvers. The left hand side (LHS) matrix consists of a 7-point stencil for the fluids points, 9-point stencil for the fringe points, and 1-point stencil for the hole points. The LHS matrix is assembled only at the first time step as grids are static, and the right hand side (RHS) vector is updated every time step. The pressure Poisson equation for the fluid points are:

$$\Delta V\left[\frac{\partial}{\partial x} grad_x P^{(n+1)} + \frac{\partial}{\partial y} grad_y P^{(n+1)} + \frac{\partial}{\partial z} grad_z P^{(n+1)}\right] = \Delta V \frac{1}{\Delta t}\left(\frac{\partial u}{\partial x} + \frac{\partial v}{\partial y} + \frac{\partial w}{\partial z}\right) \tag{12}$$

where ΔV is the grid volume, and $P^{(n+1)}$ is the pressure at time step $(n+1)$. For the Cartesian grid the gradients are computed as below:

$$\frac{\partial}{\partial x} grad_x P^{(n+1)} = \underbrace{\frac{1}{\rho_{i+\frac{1}{2}}}\frac{1}{\Delta x_{i+\frac{1}{2}}}}_{C11} P_{i+1,jk} - \underbrace{\left(\frac{1}{\rho_{i+1/2}}\frac{1}{\Delta x_{i+1/2}} + \frac{1}{\rho_{i-1/2}}\frac{1}{\Delta x_{i-1/2}}\right)}_{D1} P_{ijk} + \underbrace{\frac{1}{\rho_{i-1/2}}\frac{1}{\Delta x_{i-1/2}}}_{C12} P_{i-1,jk} \tag{13a}$$

$$\frac{\partial}{\partial y} grad_y P^{(n+1)} = \underbrace{\frac{1}{\rho_{j+\frac{1}{2}}}\frac{1}{\Delta y_{j+\frac{1}{2}}}}_{C21} P_{i,j+1,k} - \underbrace{\left(\frac{1}{\rho_{j+1/2}}\frac{1}{\Delta y_{j+1/2}} + \frac{1}{\rho_{j-1/2}}\frac{1}{\Delta y_{j-1/2}}\right)}_{D2} P_{ijk} + \underbrace{\frac{1}{\rho_{j-1/2}}\frac{1}{\Delta y_{j-1/2}}}_{C22} P_{i,j-1,k} \tag{13b}$$

$$\frac{\partial}{\partial z} grad_z P^{(n+1)} = \underbrace{\frac{1}{\rho_{k+\frac{1}{2}}}\frac{1}{\Delta z_{k+\frac{1}{2}}}}_{C31} P_{i,j,k+1} - \underbrace{\left(\frac{1}{\rho_{k+1/2}}\frac{1}{\Delta z_{k+1/2}} + \frac{1}{\rho_{k-1/2}}\frac{1}{\Delta z_{k-1/2}}\right)}_{D3} P_{ijk} + \underbrace{\frac{1}{\rho_{k-1/2}}\frac{1}{\Delta z_{k-1/2}}}_{C32} P_{i,j,k-1} \tag{13c}$$

where the diagonal component of the LHS matrix is $D = \Delta V(D1 + D2 + D3)$, and the 6 non-zero coefficients $C1 - C6$ of the matrix are $\Delta V * C11, \Delta V * C21, \Delta V * C21, \Delta V * C22, \Delta V * C31\ and\ \Delta V * C32$, respectively. The LHS matrix for the orthogonal curvilinear grid solver is obtained similarly, which also consists of 7-point stencil. The pressure is interpolated for the fringe points:

$$P_{i,j,k} = W1 \times P_{d1} + W2 \times P_{d2} + W3 \times P_{d3} + W4 \times P_{d4} + W5 \times P_{d5} + W6 \times P_{d6} + W7 \times P_{d7} + W8 \times P_{d2} \tag{14}$$

where i,j,k is the fringe point index, d1- d8 are the donor points, and W1-W8 are interpolation weights. For the hole points:

$$P_{i,j,k} = 0 \tag{15}$$

The LHS and RHS matrices are assembled using distributed array module to map local data in each processor to PETSc vectors and matrices as below:

$$
\underbrace{\begin{array}{r}
Fluid \rightarrow \\
Overset \rightarrow \\
Blanked \rightarrow \\
Fluid \rightarrow \\
Overset \rightarrow
\end{array}
\left[\begin{array}{cc}
\overbrace{\boxed{\begin{array}{c}\cdots C1..C2..C3..D..C4..C5..C6\ldots \\ \ldots\ldots.1\ldots\ldots\ldots \\ \ldots\ldots.1\ldots\ldots\ldots\end{array}}}^{Cartesian} & \begin{array}{c}\ldots\ldots.0\ldots\ldots\ldots \\ \cdots -W1..-W2\ldots\ldots..-W7..-W8\ldots. \\ \ldots\ldots.0\ldots\ldots\ldots\end{array} \\
\begin{array}{c}\ldots\ldots.0\ldots\ldots\ldots \\ \cdots W1..W2\ldots\ldots..W7..W8\ldots.\end{array} & \underbrace{\boxed{\begin{array}{c}\cdots C1..C2..C3..D..C4..C5..C6\ldots \\ \ldots\ldots.1\ldots\ldots\ldots\end{array}}}_{Orthogonal\ Curvilinear}
\end{array}\right]}_{LHS}
\begin{bmatrix} P_{Fluid} \\ P_{Overset} \\ P_{balnked} \\ P_{Fluid} \\ P_{Overset} \end{bmatrix}
=
\underbrace{\begin{bmatrix} div(u) \\ 0 \\ 0 \\ div(u) \\ 0 \end{bmatrix}}_{RHS}
\tag{16}
$$

The above linear system is solved using Krylov subspace based GMRES iterative method with ASM preconditioner.

The standard Smagorinsky subgrid-scale model with model constant C_S = 0.01 is used for the turbulence modeling, as dynamic model constant evaluation results in large difference in the eddy viscosity across the overset region due to secondary filtering. Even with the standard dynamic approach up to 10% discontinuity in eddy viscosity is observed across the overset region due to the differences in the grid volume in two solvers.

The sharp density jump across the interface caused sudden divergence close to the overset region especially for the air-points very close to the interface surrounded by water points. Thus to avoid such instabilities the density is smoothed similar to viscosity over a thin transition band across the interface.

The numerical approach is same as that of the Cartesian and curvilinear grid solvers, except the convection terms discretization which is dropped to 3rd order QUICK scheme for the orthogonal curvilinear solver. The order of convection term is dropped as the overset interpolation is obtained only for 2 J-planes, whereas 5th order discretization requires interpolation for 3 J-planes. Both the solvers use MPI based domain decomposition for solution on parallel processors, and use MPI-I/O. The coupled solutions from the solvers written in Tecplot format for visualization purposes.

III. Simulation Conditions, Validation Data, Domain, Grids and Boundary Conditions

Flow over a circular cylinder is an ideal case for V6.2 validation as it involves orthogonal curvilinear boundary layer grids. Such flows involve complex phenomenon such as separation, reattachment or vortex shedding and exhibits vastly different behavior on *Re*. A steady laminar flow exists up to Re ~ 40 with a pair of symmetric counter-rotating vortices attached behind the cylinder. With the increase in Re, a laminar vortex shedding, known as Karman vortex sheet, is observed behind the cylinder. The shear layer separating from the cylinder becomes unstable around *Re* = 1200 resulting in three-dimensional turbulent wake behind the cylinder. Flow up to *Re* = 2×10^5 exhibits laminar boundary layer flow before the separation and is referred to as sub-critical regime. For higher *Re* the boundary layer on the cylinder becomes turbulent even before separation and is referred to as super-critical region. The flow past an interface piercing cylinder has received much less attention compared to the single phase counterpart. In general, the free surface adds great complexities to the flow due to the generation of waves in various forms and their interaction with the body and vortices, the air–water interfacial effects like bubble entrainment and surface tension, and the three-dimensional flow separation. In this study, laminar simulations are performed for Re = 40 and 200, turbulent flow at sub-critical *Re* = 3900 and interface piercing simulation at Re = 27,000 and Fr = 0.8.

Experimental data available for *Re* = 40 includes recirculating bubble characteristics and C_d [15,16]. The surface vorticity (ω_s) and surface pressure (P_s) predictions are also compared with the benchmark CFD results available in the open literature obtained using body-fitted grid [17] and IBM [18] solvers. No experimental data is available for *Re* = 200, but ample high resolution CFD results are available in the literature for comparison purposes [18]. The turbulent flow over a circular cylinder at sub-critical *Re* = 3900 is well studied validation case (refer to [19] and reference therein) and has detailed experimental data including mean and turbulent flow characteristics. Lourenco and Shih [20] provide detailed measurements of the mean recirculation region, drag coefficient, vortex shedding *St*, mean velocities and Reynolds stress profiles at selected streamwise locations from particle image velocimetry measurements. Limited mean velocity profile data are also available in Ong et al. [21] using hot-wire measurements. The surface pressure distribution data were procured by Norberg [22] at a slightly higher *Re* = 4020. Limited experimental data are available for *Re* = 27,000 and *Fr* = 0.8 [23] which includes mean and RMS of wave elevation and mean streamwise velocity profile at x/D_o = 4.5 aft of the cylinder. Suh et al. [10] recently performed LES of interaface percing cylinder at *Re* = 27,000 for *Fr* = 0.2 and 0.8 using V6-OC and identified the effects of interface on the vortical structure, separation pattern and separated region. Koo et al. [24] extended the study to higher *Re* = 4.6×10^5 and *Fr* = 1.64 to study the affects of *Re* and *Fr* on such flows. Additional V6-IBM and V6-OC simulations are also performed for comparsion purposes.

Table 1 provides a summary of simulations conditions performed in this paper. V6-IBM simulations are performed only for the laminar cases, as they involve inexpensive 2D grids, whereas the higher *Re* 3D simulations

would be extremely expensive and are beyond the scope of this study. V6-IBM domain size is X = [-20, 20] and Y = [-11,11], and is discretized using 204×260×3 points in X, Y and Z directions, respectively. V6-OC simulations are performed for all the cases, except for the interface piercing case for which previously published results from Suh et al. [10] are used. V6-OC simulations are performed using a O-grid with domain size = $20D_o$ in the X-Y plane. Three grid resolutions coarse (128×128×3), medium (256×128×3) and fine (512×128×3) are considered in the radial directions for *Re* = 40 simulations. The middle grid is used for the *Re* = 200 case. For *Re* = 3900 simulation, the Z domain size = [-3,3] and three different grids consisting of 1.5M, 3.1M and 12.5M points are used. Suh et al. [10] used three different grids consisting of 2.1M, 4.2M and 8.4M grids, and showed good predictions on the medium grid, thus the medium grid predictions are used for comparison.

V6-2 domain size and the background grid resolution is same as that used in V6-IBM for the laminar simulations. For *Re* = 40 case, the effect of wall-layer (WL) domain size ($0.1D_o$ to $0.2D_o$) and grid resolution is also studied to identify any limitation on the WL domain size due to overset grid interpolation. WL size of $0.2D_o$ is found to be sufficiently thin for the circular cylinder simulations and used for rest of the cases. The domain sizes are chosen same as that in V6-OC for the turbulent simulations. For *Re* = 3900 case, two different grids consisting of 1.8M and 3.7M corresponding to V6-OC coarse and medium grids are used. The grid for the interface piercing case consists of 6.1M points which corresponds to the medium grid in V6-OC in the X-Y plane, but is coarser than V6-OC in the normal direction.

A X-Y plane view of the grid domains and boundary conditions for V6-IBM, -OC and V6.2 are shown in Fig. 3. For V6-IBM uniform inlet and convective boundary conditions are specified at I-MIN and I-MAX planes, respectively. Slip wall conditions are specified at rest of the boundaries. An IBM approach is used for the wall boundary condition. For V6-OC, inlet is specified for $-30° \leq \theta \leq 30°$, and convective exit boundary conditions elsewhere for J-MAX plane. Non-slip wall boundary conditions is specified at J-MIN plane, and slip conditions for K-MIN and K-MAX planes. For V6.2, background Cartesian grid is used to specify inlet, exit and slip walls boundary condition away from the wall, and WL J-MIN plane specifies the no-slip boundary condition. The WL and background solvers communicate via the overset boundary conditions as discussed above.

Table 1: Simulation conditions for laminar, turbulent and two-phase flows over a circular cylinder.

Cases	*Re, Fr*	Solver	Domain Size	WL domain	Grid	Grid resolution		Results
						$N_x \times N_y \times N_z$	$N_r \times N_\theta \times N_z$	
Single-phase Laminar flow	40, -	V6-IBM	X=[-20,20]D_o, Y = [-11,11]D_o	-	-	204×260×3	-	• Steady recirculation • Compare with V6-OC, V6-IBM and EFD [15, 16] and CFD in literature [17, 18] • Effect of WL domain size • Effect of WL grid resolution
		V6-OC	O-Grid, R = $20D_o$	-	Coarse	-	128×128×3	
					Medium	-	256×128×3	
					Fine	-	512×128×3	
		V6.2	X=[-20,20]D_o, Y = [-11,11]D_o	$0.2D_o$	Coarse WL	204×260×3	13×128×3	
					Medium WL	204×260×3	22×128×3	
					Fine WL	204×260×3	32×128×3	
				$0.15D_o$	Fine WL	204×260×3	24×128×3	
				$0.1D_o$	Fine WL	204×260×3	17×128×3	
	200, -	V6-IBM	X=[-20,20]D_o, Y = [-11,11]D_o	-	-	204×260×3	-	• Unsteady vortex shedding • Compare with V6-IBM, V6-OC and other CFD in literature [18]
		V6-OC	O-Grid ; R = $20D_o$	-	-	-	256×128×3	
		V6.2	X=[-20,20]D_o, Y = [-11,11]D_o	$0.2D_o$	-	204×260×3	22×128×3	
Single-phase turbulent flow	3900, -	V6-OC	O-Grid, R = $20D_o$, Z = [-3,3]D_o	-	Coarse	-	256×256×24	• LES of turbulent flows • Compare with V6-OC, CFD in literature [19] and EFD[20-22] • Effect of grid resolution
					Medium	-	256×256×48	
					Fine	-	512×512×48	
		V6.2	X=[-20,20]D_o, Y = [-20, 20]D_o, Z = [-3,3]D_o	$0.2D_o$	Coarse	288×248×24	20×256×24	
					Medium	288×248×48	20×256×48	
Two-phase turbulent flow	2.7×10^4, 0.8	V6-OC [10]	O-Grid, R = $20D_o$, Z = [-4,2]D_o		Medium	-	256×128×128	• LES of turbulent flows • Compare with V6-OC [10] and EFD[23] • Effect of air-water interface on vortices
		V6.2	X=[-20,20]D_o, Y = [-20, 20]D, Z = [-4,2]D_o	$0.2D_o$	Medium	260×228×96	20×256×96	

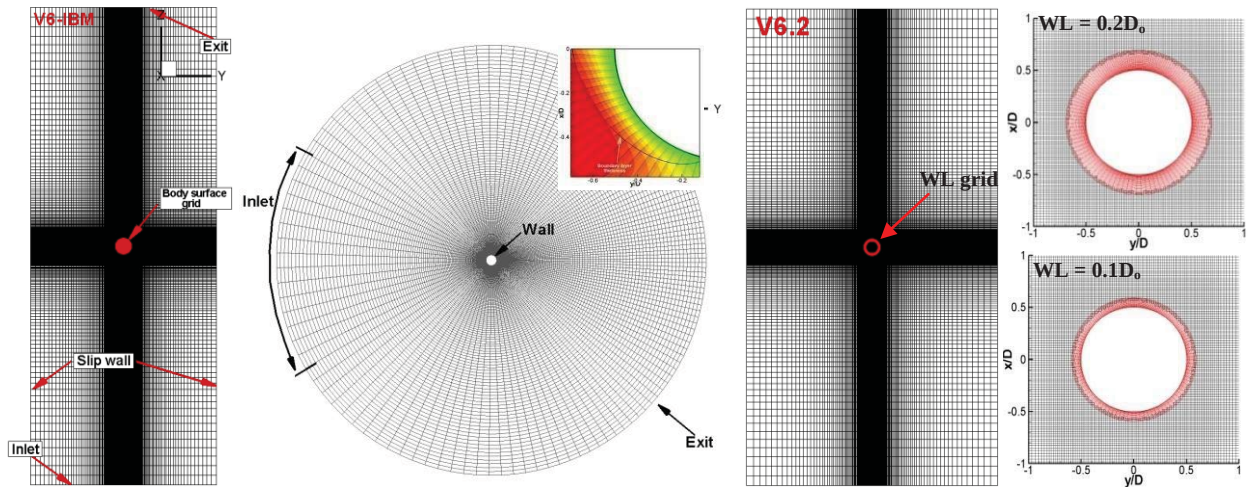

(a) (b) (c) (d)

Figure 3. Description of domain, grids and boundary conditions for (a) V6-IBM, (b) V6-OC, inset shows the boundary layer thickness for *Re* = 40, (c) V6.2, and (d) WL domain size.

IV. Validation for Flows over Circular Cylinder

A. Laminar Flows

Steady recirculating bubble behind the cylinder is predicted by all the solvers on all the grids as shown in Fig. 4. Table 1 summarizes the recirculating bubble characteristics and C_d predictions and compared with EFD data [15,16]. Recirculation bubble characteristics include the length L, location ($0.5+a$, $\pm b/2$) of the recirculating bubbles as shown in Fig. 5, and the separation angle θ (degree) is defined from the trailing edge. The surface vorticity (ω_s) and surface pressure (P_s) predictions are compared with the benchmark CFD results available in the open literature obtained using body-fitted grid [17] and IBM [18] solvers.

V6-IBM predictions for L, b and C_d compare within 2% of EFD data, but a is underpredicted by 8% and θ by 5.4%. The P_s distribution compares well with Xu Sheng [18] results which is also using an IBM solver, but the peak values are lower than that obtained by Braza et al. [17] on body fitted grids. The peak ω_s is underpredicted by 9.6% compared to benchmark CFD results. V6-OC C_d predictions are within 5.5%D of the EFD on all the grids. C_d is dominated by $C_{d,p}$ which accounts for 66% of the total. The recirculating bubble characteristics predictions compare within 13%D, 6.3%D and 4%D of the EFD data for coarse, medium and fine grids, respectively. The P_s predictions do not show any changes between the grids and the results agree very well with Braza et al. [17]. The peak ω_s predictions improves by 1.63% between coarse and medium grid, and both medium and fine grid results compare very well with Braza et al. [17] results.

V6.2 overpredicts C_d by 6.8%D on all the WL grids. The recirculating bubble characteristics and θ does not show significant dependence on WL grid resolution, where the results are within 3% of the EFD. The ω_s predictions improve by 3.07% between the coarse and medium WL grids and <1.26% between the medium and fine WL grids. The medium and fine WL grid results compare very well with the benchmark CFD data. The P_s distribution does not show dependence on WL grid resolution and compares well with Braza et al. [17]. The WL domain sizes considered for study lies within the boundary layer which extends up to 0.19D$_o$ as shown in inset figure in Fig. 3. As shown in Fig. 6, the flow pattern do not show any significant change, the recirculating bubble characteristics show <1% and C_d, θ, P_s and ω_s distributions show < 0.3% change on the domain size.

Overall, V6.2 predictions comapre well with the EFD and V6-OC, and shows 10% better P_s and ω_s predictions compared to V6-IBM as shown in Fig. 7 on the same background grid resolution.

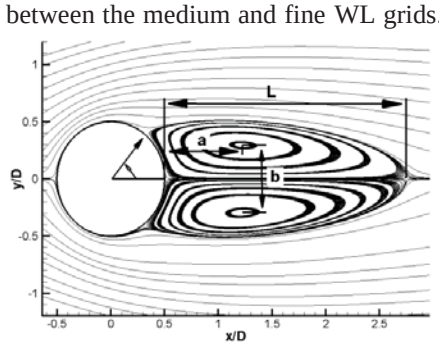

Figure 5. Definition of recirculating bubble characteristics.

Table 2: Grids, WL domain size, recirculating bubble characteristics and drag coefficients for flow past a circular cylinder at *Re* = 40.

	Grids	WL domain	*L*		*a*		*b*		Θ°		C_d		$C_{d,p}$	$C_{d,f}$
				E%*D*		E%*D*		E%*D*		E%*D*		E%*D*		
EFD (D) [15]	-	-	2.13	-	0.76	-	0.59	-	53.8	-	-	-	-	-
EFD (D) [16]			-	-	-	-	-	-	-	-	1.48	-	-	-
Xu [18]	-	-	2.21	-3.76	0.73	3.95	0.56	5.08	52.9	1.67	1.60	-8.10	-	-
V6-IBM	-	-	2.11	0.94	0.70	7.89	0.58	1.69	50.9	5.39	1.51	-2.03	0.97	0.54
V6-OC	Coarse	-	1.86	12.7	0.61	19.7	0.55	7.23	51.7	3.90	1.55	-4.73	1.01	0.54
	Medium		2.05	3.76	0.66	13.2	0.58	2.35	52.4	2.60	1.56	-5.41	1.02	0.54
	Fine		2.01	5.63	0.73	3.95	0.57	3.39	54.0	-0.37	1.56	-5.41	1.02	0.54
V6.2	Coarse WL	$0.2D_o$	2.24	-5.16	0.72	5.26	0.59	0	53.7	0.19	1.58	-6.76	1.04	0.54
	Medium WL		2.24	-5.10	0.72	5.26	0.59	0	53.7	0.19	1.58	-6.76	1.04	0.54
	Fine WL		2.24	-5.16	0.72	5.26	0.59	0	54.0	-0.37	1.58	-6.76	1.04	0.54
	Fine WL	$0.15D_o$	2.24	-5.16	0.71	6.58	0.59	0	54.2	-0.74	1.58	-6.76	1.04	0.54
	Fine WL	$0.1D_o$	2.23	-4.69	0.72	5.26	0.59	0	54.0	-0.37	1.58	-6.76	1.04	0.54

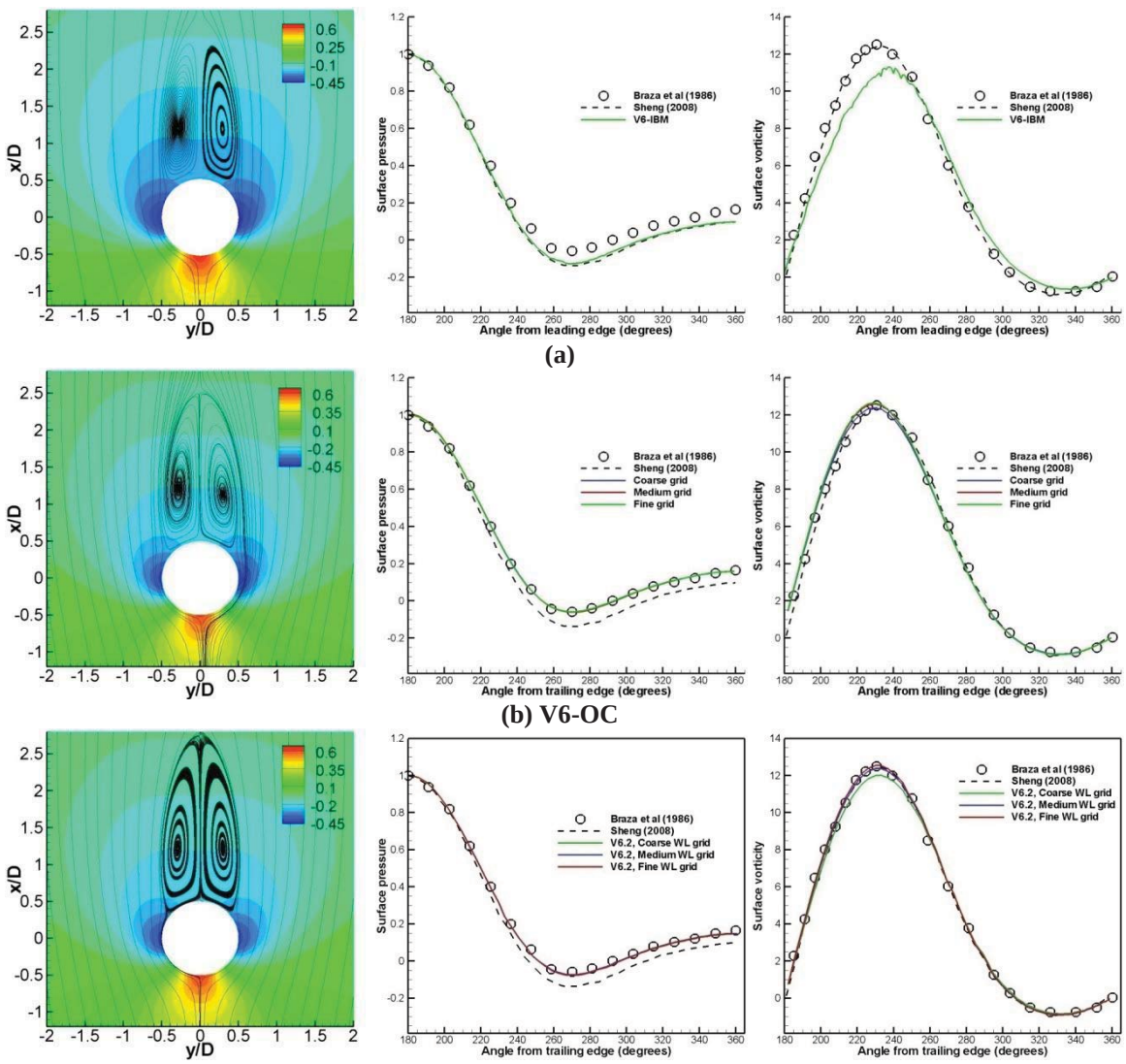

(a)

(b) V6-OC

(c) V6.2

Figure 4. Flow streamline and pressure contours (left panel), surface pressure (middle panel) and surface vorticity (right panel) profiles predicted by (a) V6-IBM, (b) V6-OC and (c) V6.2 simulations for *Re* = 40.

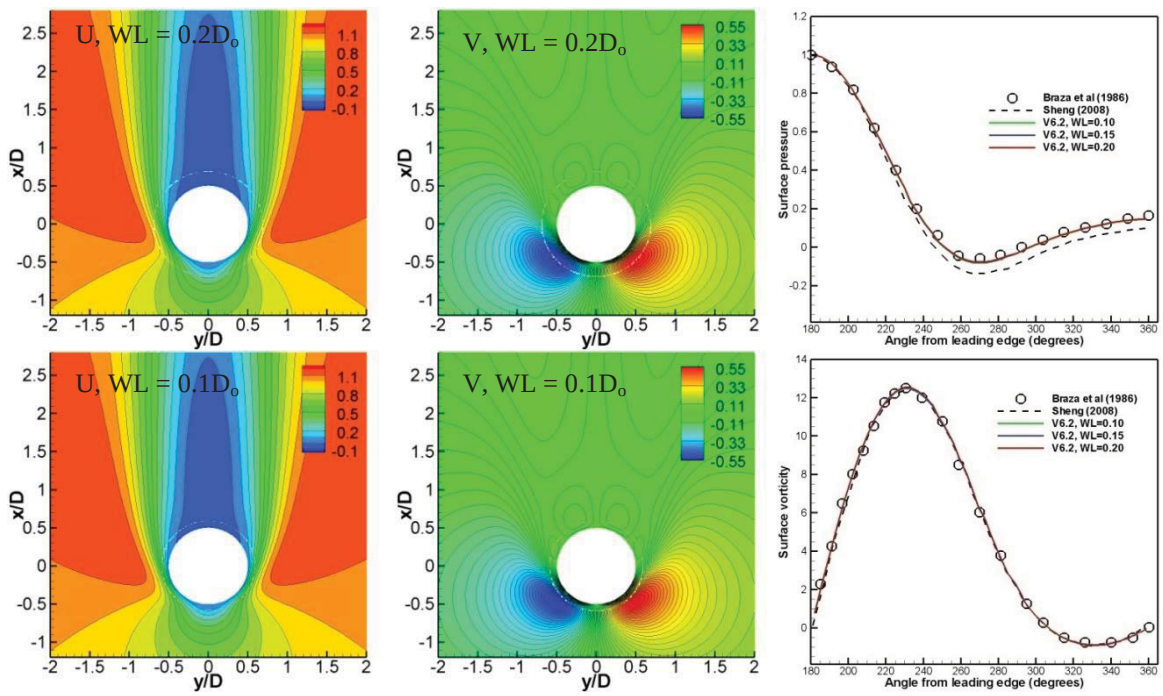

Figure 6. Contours of streamwise velocity (left panel) for WL = 0.2D$_o$ and 0.1D$_o$, contours of transverse velocity (middle panel) for WL = 0.2D$_o$ and 0.1D$_o$, surface pressure (right panel-top) and surface vorticity (right panel-bottom) predicted by V6.2 simulations for *Re* = 40.

An unsteady vortex shedding is predicted by all the solvers for *Re* = 200, V6.2 predictions are shown in Fig. 8 for demonstration. As shown in Table 3, *St* of the vortex shedding compares within 1% between the solvers and those reported by Xu [18] and averaged CFD results surveyed therein. Mean C_d is predicted within 3% of the benchmark CFD results for V6-IBM, but C_d and C_l amplitudes are under predicted by 6% as shown in Fig. 7. Mean C_d predictions are 7% and 5% lower than the EFD for V6-OC and V6.2, respectively. As shown in Fig. 9, V6-OC and V6.2 unsteady amplitudes compare within 3%.

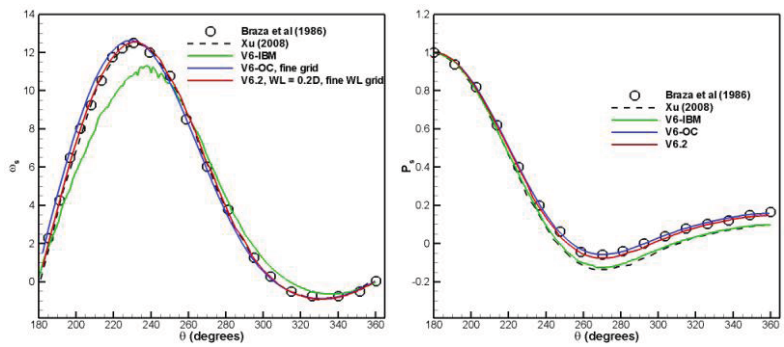

(a) (b)

Figure 7. (a) ω_s and (b) P_s predictions using V6-IBM, -OC and V6.2 for Re = 40 are compared with benchmark CFD results.

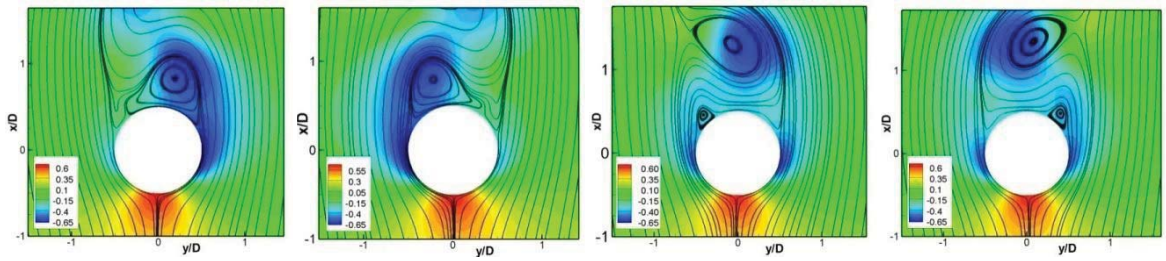

Figure 8. Quarter phases of vortex shedding obtained using V6.2 for *Re* = 200. Contours are for pressure predictions.

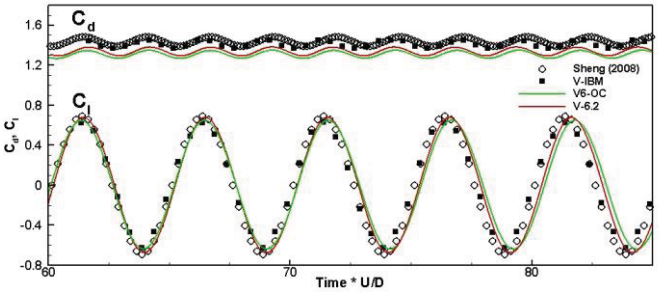

Figure 9. Time history of C_d and C_l predictions using V6-IBM, -OC and 6.2 for Re = 200 are compared with Xu [18].

Table 3: Drag and lift coefficients, and Strouhal number for flow past circular cylinder, *Re* = 200.

Cases	C_d		C_l		S_t
	Mean	Amplitude	Mean	Amplitude	
Xu [18]	1.44	0.045	0	0.68	0.201
Averaged CFD [18]	1.40	0.042	0	0.64	0.200
V6-IBM	1.41	0.040	0	0.64	0.200
V6-OC	1.32	0.041	0	0.66	0.197
V6.2	1.34	0.043	0	0.67	0.199

B. Turbulent Flows

As shown in Fig. 10, unsteady Karman vortex shedding is predicted by both V6-OC and V6.2 for Re = 3900, but unlike the laminar flow the vortices are affected largely by velocity in the normal direction parallel to the cylinder axis. The streamwise and cross flow velocities shows a negative region behind the circular cylinder and alternating positive and negative regions in the wake, corresponding to the unsteady Karman vortex shedding. V6.2 predictions are similar to V6-OC predictions close to the cylinder, but the former does not capture small scale structures further away from the cylinder due to coarse grid resolution.

Table 4 compares the mean recirculation region, drag coefficient and vortex shedding *St* predictions obtained using V6-OC and V6.2 with benchmark LES [19] and EFD data [21]. The averaging is performed both in space and time for 40 flow time, i.e., eight vortex shedding cycles, and along the normal direction. The recirculation region characteristics include the region length L, separation angle θ (degree) from the leading edge, and minimum streamwise velocity U_{min} behind the cylinder and base pressure C_{Pb} at the trailing edge. V6-OC results show that the mean recirculation length increases significantly between the coarse and medium grids, i.e., when the normal grid resolution is increases. The coarse grid results underpredict L by 20.1%D, whereas the medium grid results overpredict the length by 25%D compared to the EFD data. The overprediction of L on finer grids is consistent with benchmark LES. The flow separates early from the surface on the coarse grid, whereas good predictions are obtained on finer grids. U_{min} is predicted well on the coarse grid, but are overpredicted by up to 50%D on finer grids. A similar over prediction was observed in the benchmark LES simulation [19] and was explained due to early transition of the separated shear layer in the experiment due to external disturbances, as discussed later. C_{Pb} and C_d predictions also improve with the grid resolution, where the latter compares within 6%D of the EFD. The drag coefficient is mostly due to $C_{d,p}$ which accounts for up to 95% of the total. The unsteady vortex shedding *St* is predicted within 3%D on all the grids. The time history of the drag coefficients in Fig. 11 show higher fluctuation on the coarse grid compared to medium and fine grids, this is again due to early transition of the separated shear layer on coarse grids. Overall, the medium grid is found to be sufficiently fine for this case and further grid refinements both in the wall normal and circumferential directions do not affect the predictions significantly. The results on medium grid are comparable to those reported in benchmark LES [19].

V6.2 predictions on coarse and fine grids shows a similar trend of improvement as that observed in V6-OC. The medium grid Θ, C_{Pb}, C_d and *St* predictions are within 6.5%D, 0.1%D, 2%D and 2.3%D of the EFD, respectively. Similar to V6-OC, L is over predicted by 17%D on medium grid, and U_{min} predictions on the coarse grid compare well with the EFD but are overpredicted by 42%D on the medium grid. Again, the overpredictions of L and U_{min} are consistent with benchmark LES predictions.

Table 4: Grids, recirculation region characteristics, Strouhal number, and base suction coefficients for flow past circular cylinder, *Re* = 3900

		Grid	L		$\Theta°$		U_{min}		$-C_{Pb}$		C_d		$C_{d,p}$	$C_{d,f}$	*St*	
				E%*D*		**E%*D***		**E%*D***		**E%*D***		**E%*D***				E%*D*
EFD (D) [21]		-	1.18	-	86.0	-	-0.24	-	0.88	-	0.99	-	-	-	0.215	-
Kravchenko et al. [19]	Upwind	-	1.36	**-15.3**	85.8	**0.23**	-0.32	**-33.3**	0.95	**-7.95**	1.01	**-2.0**	-	-	0.203	**5.58**
	Central	-	1.40	**-17.0**	86.9	**-1.05**	-0.35	**-45.8**	0.93	**-5.68**	1.01	**-2.0**	-	-	0.207	**3.72**
	B-spline	-	1.35	**-14.4**	88.0	**-2.33**	-0.37	**-54.2**	0.94	**-6.8**	1.05	**-6.0**	-	-	0.210	**2.33**
V6-OC		Coarse	0.94	**20.3**	90.0	**-4.65**	-0.24	**0**	1.03	**-17.0**	1.20	**-21.2**	1.15	0.05	0.210	**2.33**
		Medium	1.50	**-25.4**	86.7	**-0.81**	-0.29	**-20.8**	0.88	**0**	0.93	**6.06**	0.88	0.05	0.210	**2.33**
		Fine	1.54	**-26.3**	86.5	**-0.58**	-0.36	**-50.0**	0.85	**3.41**	0.94	**5.05**	0.89	0.05	0.208	**3.26**
V6.2		Coarse	1.01	**15.1**	97.0	**-12.8**	-0.25	**-4.17**	0.92	**-4.55**	1.18	**-19.2**	1.13	0.05	0.208	**3.26**
		Medium	1.39	**-16.8**	91.6	**-6.51**	-0.34	**-41.7**	0.88	**0**	0.97	**2.02**	0.92	0.05	0.220	**-2.33**

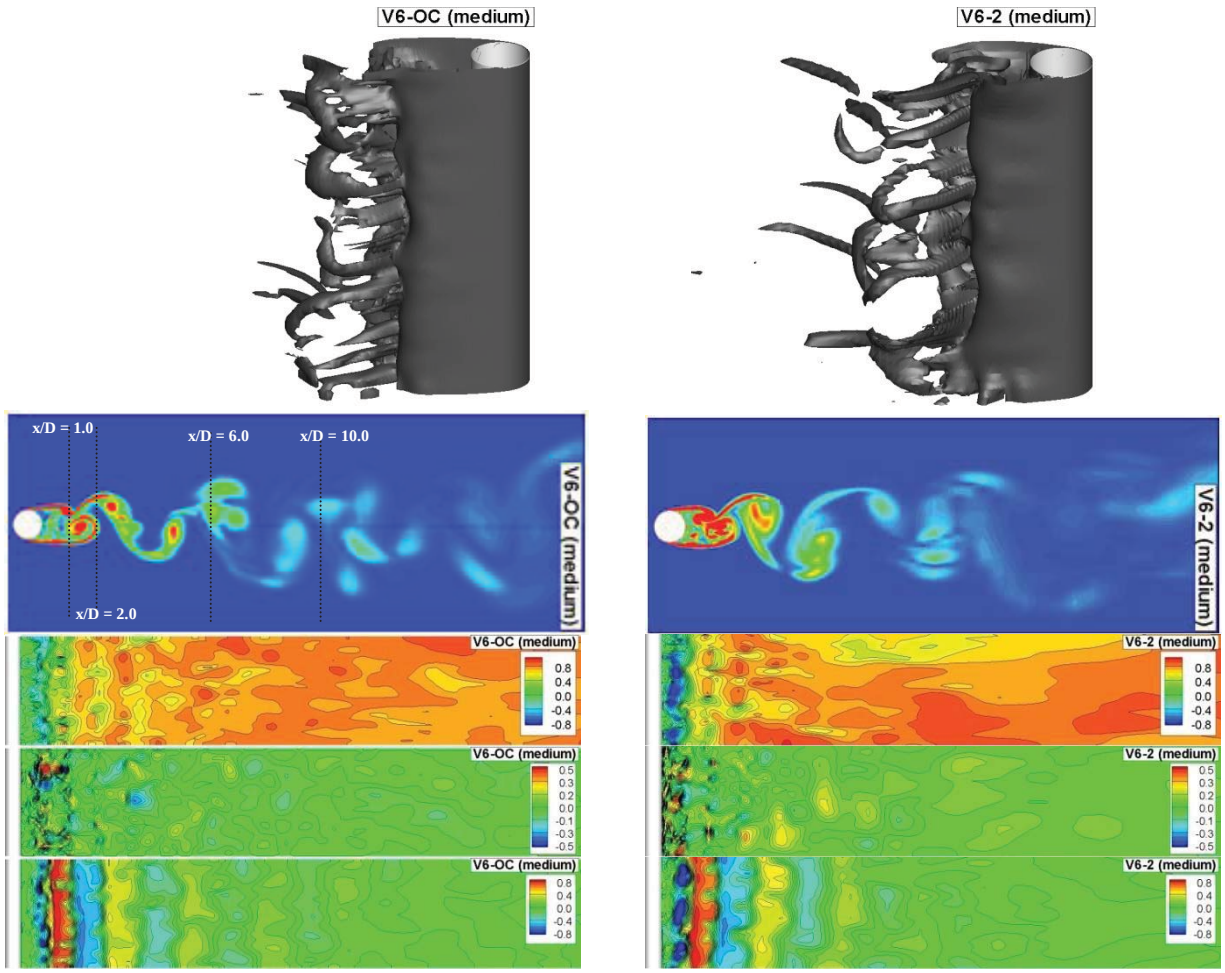

(a) (b)

Figure 10. Instantaneous flow fields in the wake behind a circular cylinder obtained using (a) V6-OC and (b) V6.2 on the medium grids for *Re* = 3900. Figures shows (from top to bottom): isosurface of instantaneous vorticity magnitude ($\omega D/U$ = 2.5), contours of instantaneous vorticity magnitude, streamwise velocity, transverse velocity, and normal velocity.

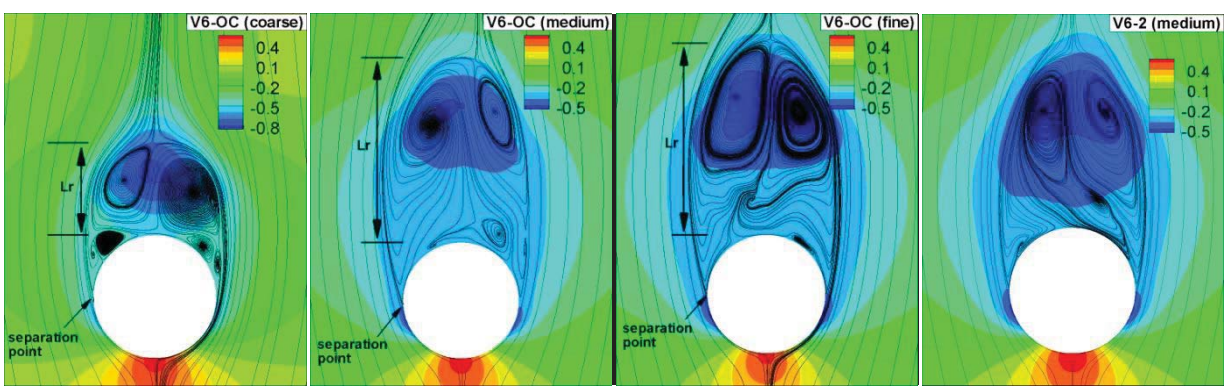

(a) (b) (c) (d)

Figure 11. Time-averaged pressure and streamlines for Re = 3900 obtained using (a) V6-OC on coarse, (b) V6-OC on medium, (c) V6-OC on fine and (d) V6.2 on medium grids.

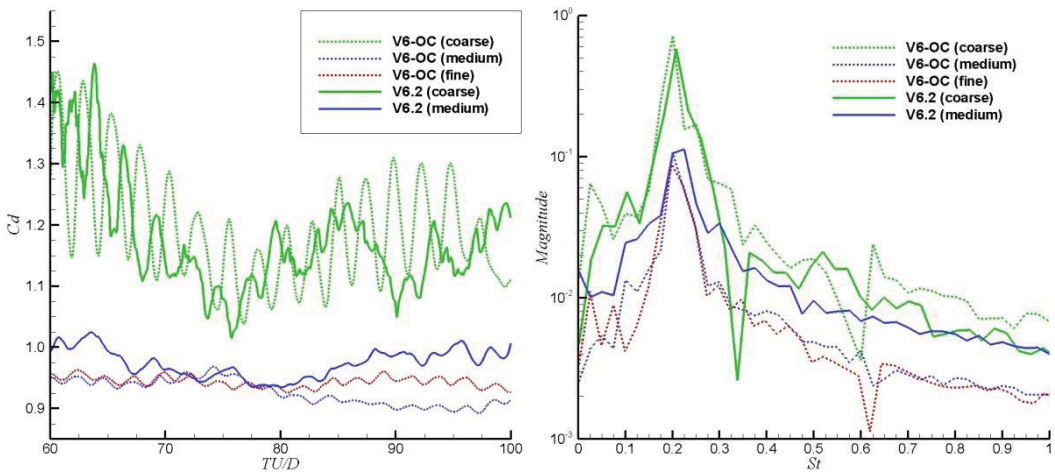

(a) (b)

Figure 12. Comparison of (a) time history of the drag coefficient and (b) FFT of the lift coefficient for the *Re* = 3900 simulations.

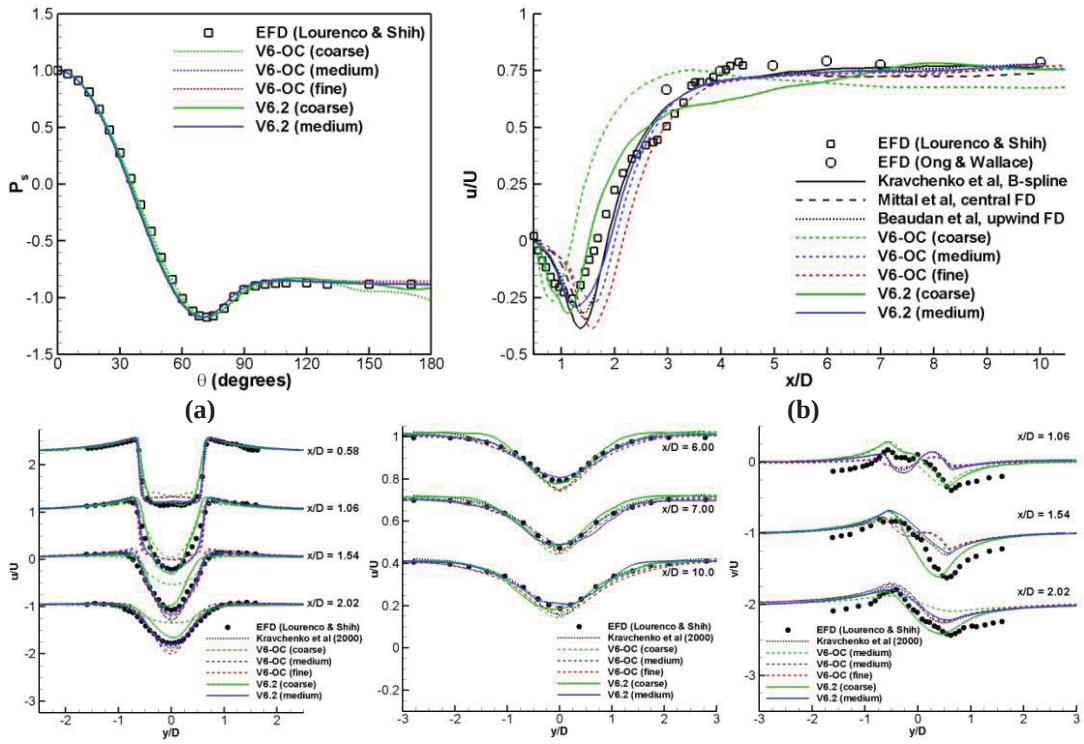

(a) (b)

(c) (d) (e)

Figure 13. Comparison of mean flow statistics between V6.2, V6-OC, benchmark LES [19], and EFD[20, 21]. (a) Pressure distribution on the cylinder surface, (b) streamwise velocity on the wake centerline, (c, d) streamwise velocity and (e) transverse velocity at several streamwise locations in the wake of the cylinder for *Re* = 3900. Some key streamwise locations are marked in Fig. 10a.

In figure 13, the mean flow statistics predicted by V6.2 and V6OC are compared with benchmark LES and EFD. V6-OC predictions show improvement in the P_s profile especially in the separated flow region, and the results compare very well with the experiments on finer grids. Overall, the streamwise velocity profile predictions improves with the grid refinement especially for $x/D_o > 2$, and no significant differences are observed between the medium and fine grid predictions. In the region close to the cylinder $x/D_o < 2$, the results on finer grids show: minimum negative velocity further aft of the cylinder compared to the EFD; a U-shaped profile whereas EFD shows a V-shaped profile for the streamwise velocity; and the transverse velocity profile on coarse grid compares better with

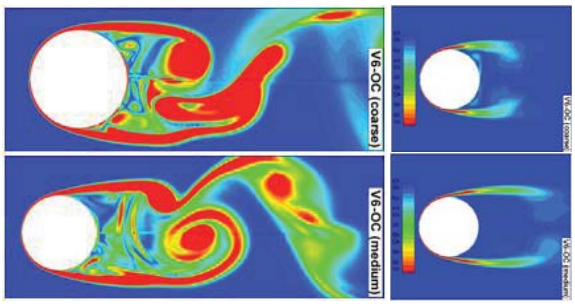

(a) (b)

Figure 14: (a) Instantaneous and (b) time averaged vorticity magnitude contours obtained using V6-OC for *Re* =3900.

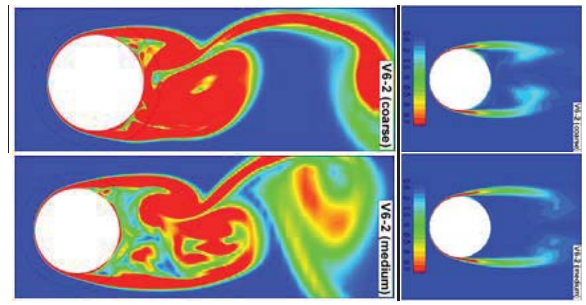

(a) (b)

Figure 15: (a) Instantaneous and (b) time averaged vorticity magnitude contours obtained using V6.2 for *Re* =3900.

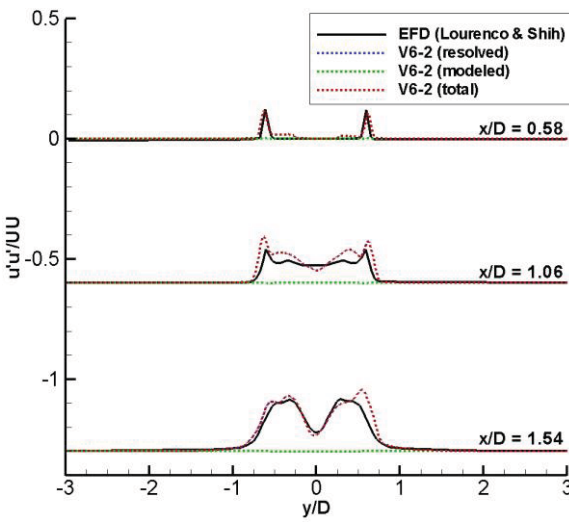

Figure 16: Reynolds stress $\overline{u'u'}$ predicted by V6.2 on medium grid for *Re* =3900.

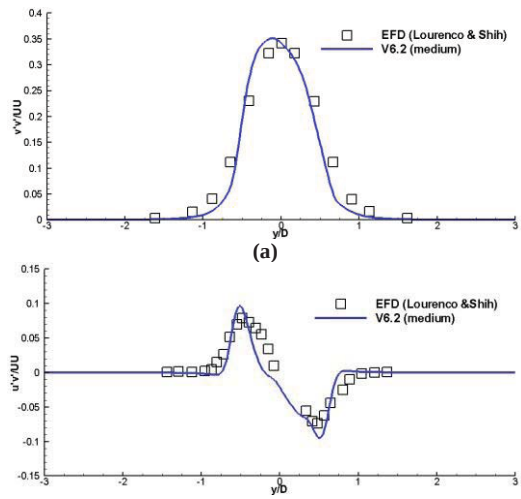

Figure 17: Reynolds stresses (a) $\overline{v'v'}$ and (b) $\overline{u'v'}$predicted by V6.2 on medium grid at x/D$_o$= 1.54 for R*e* = 3900.

the EFD than those on fine grids. The V6-OC results on finer grids compare very well with the benchmark LES results [19]. Kravchenko and Moin [19] explained the discrepancies between the EFD and CFD results due to external disturbances in the experiments. It is expected such disturbances may cause the separating shear layer to transition to turbulent closer to the cylinder resulting in shorter recirculation region and V-shaped streamwise velocity profile. As shown in Fig. 14, V6-OC simulation on coarse grid predicts significantly smaller shear layer compared to medium grid suggesting that the transition to turbulence occurs earlier on the coarse grid, consistent with Kravchenko and Moin [19] observations. Note that the difference between the coarse and medium grids is only the resolution in the normal direction, thus the resolved turbulence predictions for this case is dominated mainly by velocities in the normal direction. Further, on the coarse grid the separated flow impinges on the cylinder surface. These explain the larger unsteadiness in C_d, lower L and U_{min} and on coarse grid compared to medium grid, and discrepancies between V6-OC and EFD velocity profiles for x/D$_o$ < 2.

The trends in V6.2 coarse and medium grid predictions are similar to that observed in V6-OC simulations, i.e., shoerter separated shear layer on coarse grid (Fig. 15) resulting in smaller recirculation region and V-shaped profile close to the cylinder. P_s profile is predicted very well on the medium grid. Near the cylinder, the coarse grid wake profiles agree well with the EFD, whereas the medium grid results compare very well with the benchmark CFD. The medium grid wake predictions compare well with the EFD and benchmark CFD away from the cylinder. In Figs. 16, the streamwise Reynolds stress $\overline{u'u'}$ predictions on the medium grid is compared with EFD data close to the cylinder. As observed, the stress is dominated by the resolved components. At x/D$_o$ = 0.58, the peak stress is observed in the shear layer core, and the profiles diffuse towards the centerplane as the shear layer breaks down to small scale turbulent structure further downstream. Overall, V6.2 predictions compare well with the EFD data. The streamwise Reynolds stress predictions for x/D$_o$≥ 6 are 50-60%D lower compared to the EFD due to coarse grid

resolution. The transverse stress $\overline{v'v'}$ and shear stress $\overline{u'v'}$ predictions from V6.2 on medium grid at $x/D_o = 1.54$ are compared in Fig. 17. $\overline{v'v'}$ profile show a peak towards the centerplane, whereas $\overline{u'v'}$ profile shows almost a linear decreases in between the positive and negative values on two sides. For these components too, V6.2 predictions are in good agreement with the EFD.

C. Two-phase Turbulent Flows

Suh et al. [10] performed LES of the flow past an interface piercing circular cylinder at $Re = 2.7\times10^4$ and the $Fr = 0.2$ and 0.8 using V6-OC. The mean and RMS of interface elevation and the profiles of the mean streamwise velocities at several streamwise centerplane locations compared very well with the EFD [23] and benchmark LES simulation [26]. The study showed that the vortical structures are significantly affected by the interface. In the deep water, organized periodic vortex shedding is observed similar to the single phase case. But near the interface, the organized vortex shedding is attenuated and small-scale vortices are inclined along the interface. The two shear layers, on either side of the cylinder, deviate from the symmetric vertical plane and there are no direct interactions between them. The size of the separated region is substantially increased in the streamwise and transverse directions, and the separation is enhanced due to the reduced adverse pressure gradient by the negative interface slope along the cylinder. The streamwise vorticity and outward transverse velocity generated near the edge of the separated region were primarily responsible for the increased width of the separated region and the destruction of the periodic vortex shedding at the interface. The vertical and transverse gradients of $(\overline{v'v'} - \overline{w'w'})$ is the main source of the streamwise vorticity and the outward transverse velocity at the interface. The generation of the turbulence kinetic energy is mostly at the edge of separated flow region.

Herein, preliminary V6-2 results for $Re = 2.7\times10^4$, $Fr = 0.8$ on a similar size grid as that used in V6-OC middle grid are presented. The results are referred to as preliminary, as thus far solution has been obtained only up to 30 flow time and last 10 flow time results are used for averaging. Suh et al. [10] reported that it takes about 80 flow time to reach statistically steady state, and used another 80 flow time solution to obtain averaged solution. Thus the objective is not to validate V6.2 predictions but to discuss the solution trends early on in the simulation.

The V6.2 wave elevation pattern on the cylinder surface in Fig. 18 shows a large amplitude bow wave followed a negative interface slope up to point where shear layer starts to separate and almost uniform wave elevation in the separated region. The wave elevation pattern on the cylinder surface compares qualitatively well with the V6-OC predictions. However, the unsteadiness in the V6.2 interface behind the cylinder is much smaller than the in V6-OC, and the Kelvin wave patterns have not yet developed. Similar deficiency is observed in Fig. 19, where the Kelvin wave angle is smaller than that in EFD and the peak of the Kelvin wave is not observed. The wave elevation in the wake region is much higher than both in V6-OC and EFD. As shown in Fig. 20, the mean velocities are significantly lower in the wake region compared to both V6-OC and EFD data. The comparisons between V6-OC and V6.2 streamwise and transverse velocity profiles at $x/D_o = 1.06$ are encouraging, suggesting that large difference further downstream could be due to under-developed flow.

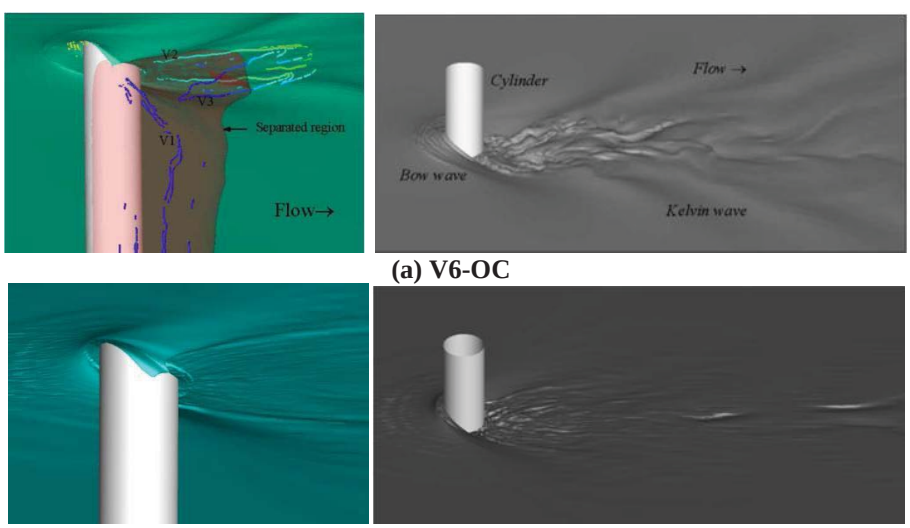

(a) V6-OC

(b) V6.2

Figure 18: Instantaneous interface elevation predictions using (a) V6-OC, Suh et al. [10]and (b) V6.2.

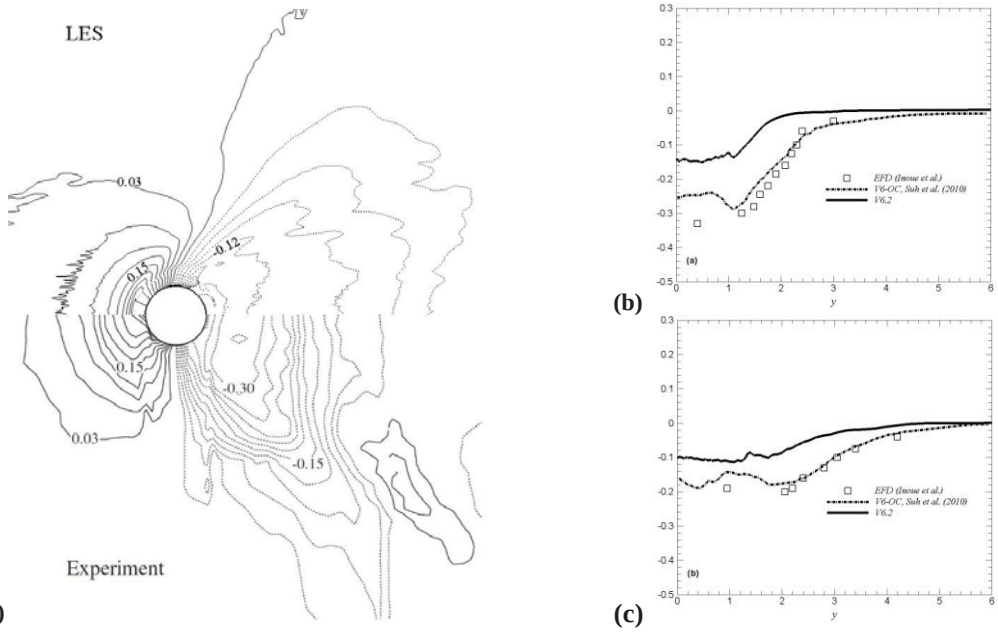

Figure 19: V6.2 mean interface elevation (a) contour, and profiles at (b) $x/D_o = 0.9$ and (c) $x/D_o = 2.0$ are compared with EFD data and V6-OC predictions.

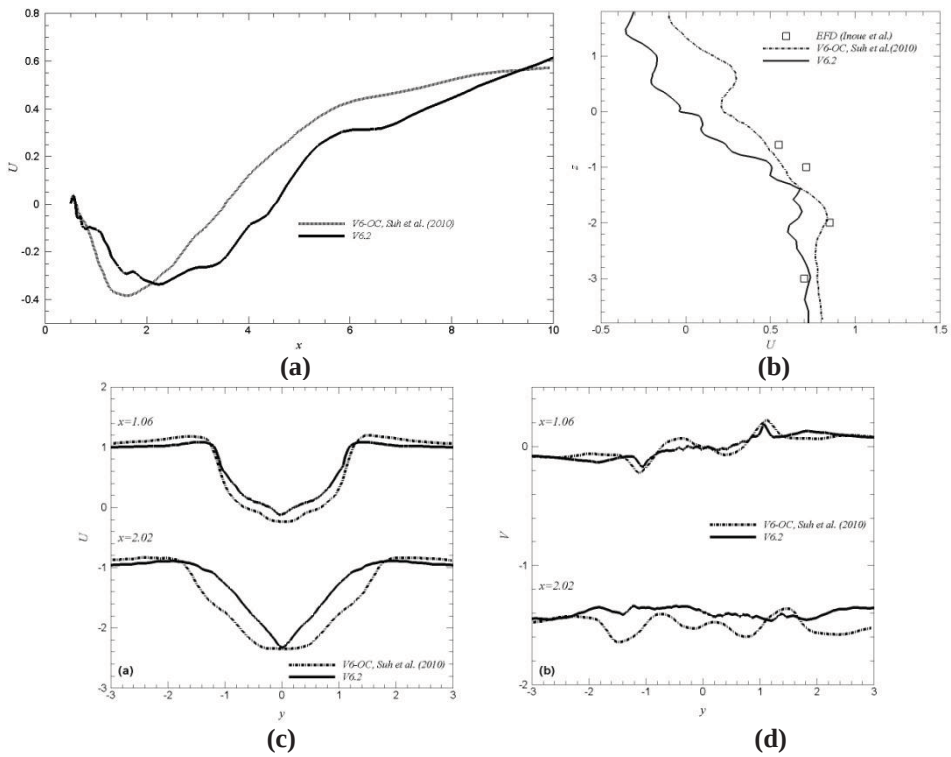

Figure 20: Mean streamwise velocity (a) on the interface along centerline y = 0, (b) vertical profile at x/D_o = 4.5, y = 0 and (c) in the wake at x/D_o = 1.06 and x/D_o = 2.02. (d) Transverse velocity profile in the wake at x/D_o = 1.06 and x/D_o = 2.02. The results are compared with EFD data and V6-OC predictions.

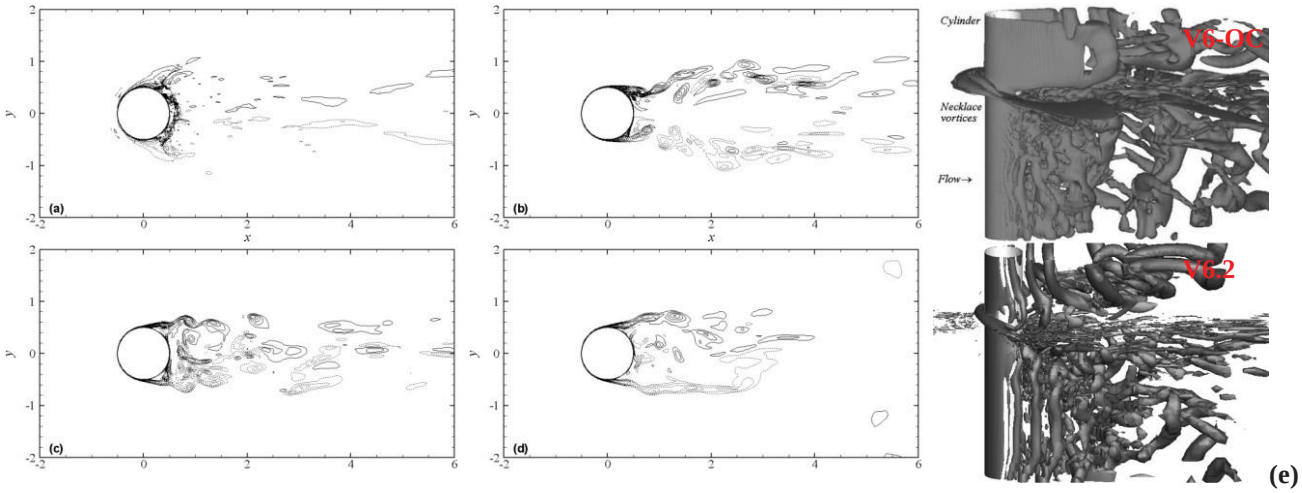

Figure 21: Instantaneous vertical vorticity contours: (a) on the interface; (b) z/D_o = -0.5; (c) z/D_o = -1; (d) z/D_o = -3.5 predicted by V6.2. Contour interval is 1.2. (e) V6-OC and V6.2 instantaneous vortical structures identified by the normalized helicity Q = 2.0 are compared.

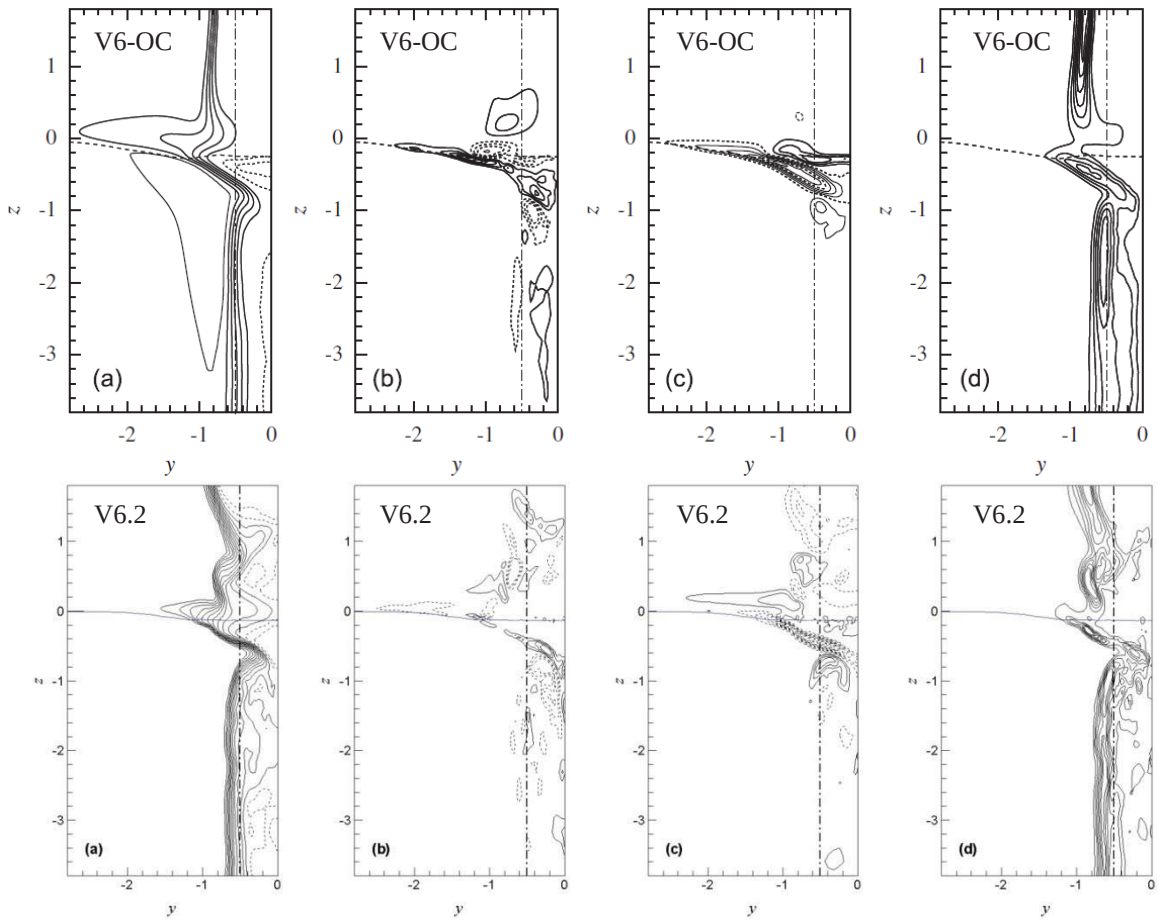

Figure 22: Contours of the mean flow at x/D_o = 1.0 plane: (a) streamwise velocity; (b) streamwise vorticity; (c) transverse vorticity; and (d) vertical vorticity. Top panel V6-OC and bottom panel V6.2. The line across the figures shows the interface, and the vertical line shows the cylinder edge.

The contours of the instantaneous vertical velocity at several planes in the deep water and at the interface in Fig. 21, shows a well defined shear layer in the deep water similar to the single phase case. As the interface is approached, the shear layer becomes unstable and breaks down. Further the shear layers on both the side starts to diverge away from the center plane, leading to the formation of Kelvin wave pattern. The isosurface of normalized helicity Q = 2.0 shows elongated quasi-vertical vortices in the deep water, which breaks down near the interface resulting in vortical structures aligned with the interface. These predictions compare qualitative well with V6-OC predictions. However, the inception of bow necklace vortices are not observed.

In Fig. 20, the wake and vorticity profiles at x/D_o = 1.0 are compared with V6-OC. V6.2 wake profile predictions correlate well with the location of the vortices. The streamwise vorticity shows two vortices with alternating vortices behind the cylinder wake and counter rotating vortices near interface at y = -1.0. The transverse vorticity shows strong vortices (compared to streamwise component) close to the interface. The vertical vorticity components shows large values in the shear layer region in deep water, and vortices inclined outward in the transverse direction in the interface. Overall comparison of the vortical structure with V6-OC predictions are good, except that the magnitudes of the third streamwise vortex behind the cylinder close to the interface and the streamwise vortices around y = -1 are lower in V6.2. Suh et al. [10] explained that these vortical structures are responsible for the attenuation of the vortex shedding and enlargement of the wake width near the interface.

Overall, the Kelvin wave pattern are captured in the preliminary V6.2 results as they are not yet fully developed. Nonetheless, the results are encouraging as the interaction of the interface and vortical structures are similar to that predicted by V6-OC. Although a fully converged solution will help evaluate the limitations of the V6.2, but preliminary simulation suggests that the current grid resolution, especially in the normal direction, is not sufficient to capture the bow necklace type vortices. Additional simulation using 128 point in vertical direction, as used in V6-OC, will be performed. Further, discrepancies between V6.2 and V6-OC are expected as: (1) the density is smoothed across the interface in V6.2, whereas V6-OC uses a sharp jump; and (2) V6.2 uses standard Smagorinsky model, whereas V6-OC uses a dynamic Smagorinsky model, and the latter is more accurate than the former. A fully converged solution may help evaluate limitations of V6.2 due to above assumption.

V. Conclusion

A wall-layer model for Cartesian grid solver is developed by coupling an orthogonal curvilinear grid solver using overset grid interpolation and coupled pressure Poisson solver. A thin wall-layer grid is used for the coupling, sufficient to resolve the boundary layer. Validation is performed for flow over a circular cylinder over a range of Reynolds number, including 2D laminar flow at Re = 40 and 200, LES of turbulent flow at subcritical Re = 3900, and LES simulation of surface piercing circular cylinder at Re=2.7×10^4, Fr=0.8. Wall-layer domain size and grid resolution studies are performed for the Re = 40 case, and grid refinement study is performed for Re = 3900 case. The results are compared with Cartesian grid IBM solver for the laminar cases, orthogonal curvilinear grid solver, benchmark CFD results available in literature and EFD data. The LES simulations are performed using standard Smagorinsky model, as the secondary filtering in the dynamic approach results in discontinuous eddy viscosity in the overset region.

The Re = 40 case exhibits attached recirculation bubble, and the recirculating bubble characteristics are predicted within 3% of the experiment. C_d predictions are 6.8% higher compared to the EFD, but agrees well with the benchmark CFD. The Re = 200 case exhibits unsteady Karman vortex shedding. The mean C_d, amplitude of resistance coefficients and St are predicted within 4.3%, 2% and 1% of benchmark CFD, respectively. Results show only 3% improvements on wall-layer grid refinement as the flow considered is laminar, and does not show sensitivity on the wall-layer domain size. The latter suggests that even thinner wall-layer grid can be used without losing accuracy, but would require finer grids in the circumferential direction for proper overset interpolation. Cartesian grid solver with wall-layer shows up to 10% improvement in surface vorticity and pressure distribution for Re = 40, and up to 3% improvement in lift and drag coefficient amplitudes for Re = 200 compared to Cartesian grid IBM solver on the same background grid.

Unsteady vortex shedding is predicted for Re = 3900 case. The mean C_d and unsteady Karman vortex shedding predictions compare within 2.5% of the experimental data. The mean recirculation characteristics are overpredicted compared to the experiments, but compare within 5% of the benchmark CFD results. The wake predictions close to the cylinder compare better with EFD on coarse grid, whereas the finer grid predictions with well resolved turbulence compare better with benchmark CFD results. This trend is expected as both the coarse grid and EFD exhibit early transition of the shear layer resulting in significantly smaller recirculation region. The wake predictions further away from the cylinder compares well with both EFD and benchmark CFD.

Preliminary results for a surface piercing cylinder are presented to discuss the solution trends early on in the solution. The Kelvin wave pattern are not captured as the flow is not yet converged. Nonetheless, the results are encouraging as the interaction of the interface and vortical structures are similar to that predicted by the orthogonal curvilinear grid solver. The results also suggest that the current grid resolution may not be sufficient to accurately predict the flow, thus simulation of finer grids are planned. A fully converged solution, expected to be available for the conference presentation, may help evaluate limitations of the wall-layer model due to the density smoothing across the interface and/or use of standard Smagorinsky model. Next, the wall-layer model will be applied for fixed sinkage and trim Wigley hull simulation at Re=2.2×10^6, Fr=0.267 [27], and the limitations of the orthogonal grid assumption will be evaluated.

Acknowledgments

This research is sponsored by the Office of Naval Research under Grant N00014-01-1-0073 and N00014-06-1-0420, under the administration of Dr. Patrick Purtell. The authors would also like to thank Dr. Pablo Carrica for his valuable suggestions and help.

References

[1]Yang, J., and Stern, F., "Sharp interface immersed-boundary/level-set method for wave-body interactions," *Journal of Computational Physics*, Vol. 228, No. 17, 2009, pp. 6590-6616.

[2]Ghias, R., Mittal, R. and Dong, H. A., "Sharp Interface Immersed Boundary Method for Compressible Viscous Flows," *Journal of Computational Physics*, Vo. 225, 2007, pp. 528-553.

[3]Stern, F., Bhushan, S., Carrica, P. and Yang, J., "Large scale parallel computing and scalability study for surface combatant static maneuver and straight ahead conditions using CFDShip-Iowa," 21st Parallel CFD Conference, 18-22 May, Moffett Field, California, 2009.

[4]Piomelli, U., "Wall layer models for LES," 46th AIAA Aerospace Science Meeting and Exhibit, 7-10 January, Reno, Nevada, 2008.

[5]Schluter, J. U., Wu, X., Kim, S., Alonso, J. J., and Pitsch, H., "Integrated RANS-LES of realistic gas turbine compressor/combustor assemble, Annual Research Briefs," Center of Turbulence Research, 2004.

[6]Zhang, L. P., Chang, X. H,, Duan, X. P., Wang, Z. Y., and Zhang, H. X., "A block LU-SGS implicit unsteady incompressible flow solver on hybrid dynamic grids for 2D external bio-fluids simulation," *Computers and Fluids*, Vol. 38, 2008, pp. 290-308.

[7]Noack, R.W., "SUGGAR: a general capability for moving body overset grid assembly," 17th AIAA Computational Fluid Dynamics Conference, Toronto, Ontario, Canada, 2006.

[8]Carrica, P. M., Wilson, R. V., and Stern, F., "An unsteady single-phase level set method for viscous free surface flows," *International Journal of Numerical Methods in Fluids*, Vol. 53, No. 2, 2007, pp. 229-256.

[9]Balay, S., Buschelman, K., Gropp, W., Kaushik, D., Knepley, M., Curfman, L., Smith, B. and Zhang, H., "PETSc User Manual," ANL-95/11, Revision 2.1.5, Argonne National Laboratory, 2002.

[10]Suh, J., Yang, J., and Stern, F., "The Effect of Air-Water Interface on the Vortex Shedding from a Vertical Circular Cylinder," in press *Journal of Fluids and Structures*, 2010.

[11]Wang, Z., Yang, J. and Stern, F., "An improved particle correction procedure for the particle level set method," *Journal of Computational Physics*, Vol. 228, No. 16, 2008, pp. 5819-5837.

[12]Wang, Z., Yang, J., Koo, B., and Stern, F., "A coupled level set and volume-of-fluid method for sharp interface simulation of plunging breaking waves," *International Journal of Multiphase Flow*, Vol. 35, No. 3, 2009, pp.227-246.

[13]Sussman, M., Smereka, P., Osher, S., "A level set approach for computing solutions to incompressible two-phase flow," *Journal of Computational Physics*, Vol. 114, No. 1, 1994, pp. 146-159.

[14]Yang, J., et al., "Large eddy simulation of ship flows with wall-layer models on Cartesian grids," 27th Symposium on Naval Hydrodynamics, Seoul, Korea, 2008.

[15]Coutanceau, M. and Bouard, R., "Experimental determination of the main features of the viscous flow in the wake of a circular cylinder in uniform translation. Part 1. steady flow," *Journal of Fluid Mechanics*, Vol. 79, 1977, pp. 231-256.

[16]Tritton, D. J., "Experiments on the flow past a circular cylinder at low Reynolds numbers," *Journal of Fluid Mechanics*, Vol. 6, 1959, pp. 547-567.

[17]Braza, M., Chassaing, P., and Minh Ha-H., "Numerical study and physical analysis of the pressure and velocity fields in the near wake of a circular cylinder," *Journal of Fluid Mechanics*, Vol. 165, 1986, pp. 79-130.

[18]Xu, S., The immersed interface method for simulating prescribed motion of rigid objects in an incompressible viscous flow," *Journal of Computational Physics*, Vol. 227, 2008, pp.5045-5071.

[19]Kravchenko, A. G., and Moin, P., "Numerical studies of flow over a circular cylinder at Re_D = 3900," *Physics of Fluids*, Vol. 12, No. 2, 2000, pp. 403-417.

[20]Lourenco, L. M., and Shih, C., "Characteristics of the plane turbulent near wake of a cylinder. A particle image velocimetry study," data taken from Kravchenko and Moin (2000) and Hansen and Forsythe (2004).

[21]Ong, L., and Wallace, J., "The velocity field of the turbulent very near wake of a circular cylinder." *Exp. Fluids*, Vol. 20, 1996, pp. 441-453.

[22]Norberg, C., "An experimental investigation of the flow around a circular cylinder: influence of aspect ratio," J. Fluid Mechanics, Vol. 258, 1994, pp. 275 - 278.

[23]Inoue, M., Bara, N., Himeno, Y., "Experimental and numerical study of viscous flow field around an advancing vertical circular cylinder piercing a free-surface," Journal of the Kansai Society of Naval Architects, Vol. 220, 1993, pp. 57–64.

[24]Koo, B., Suh, J., Yang, J. and Stern, F., "Simulations of two-phase flow past a vertical surface-piercing circular cylinder," Proceedings of ASME 2010 3rd Joint US-European Fluids Engineering Summer Meeting, FEDSM 2010, August 2-4, Montreal, Canada.

[25]Hansen, R. P. and Forsythe, J., "A grid convergence study of a highly separated turbulent flow," Computing in Science and Engineering, November/October 2004, pp. 30 -37.

[26]Kawamura, T., Mayer, S., Garapon, A., Sorensen, L., "Large eddy simulation of a flow past free surface piercing circular cylinder," ASME Journal of Fluids Engineering, Vol. 124, pp. 91-101.

[27]Sakamoto, N., Wilson, R., and Stern, F., “RANS Simulations for High-Speed Ships in Deep and Shallow Water,” Journal Ship Research, Vol. 5, No. 3, 2007, pp. 187-203